

First-principles investigation of the valley and electrical properties of carbon-doped α-graphyne-like BN sheet

Bo Chen(陈波), Xiang-Qian Li(李向前), Lin Xue(薛林), Yan Han(韩燕), Zhi Yang(杨致), Long-Long Zhang(张龙龙)
Citation: Chin. Phys. B, 2021, 30 (**5**): 057101. DOI: 10.1088/1674-1056/abddac
Journal homepage: http://cpb.iphy.ac.cn; http://iopscience.iop.org/cpb

What follows is a list of articles you may be interested in

Investigation of electronic, elastic, and optical properties of topological electride Ca_3Pb via first-principles calculations

Chang Sun(孙畅), Xin-Yu Cao(曹新宇), Xi-Hui Wang(王西惠), Xiao-Le Qiu(邱潇乐), Zheng-Hui Fang(方铮辉), Yu-Jie Yuan(袁宇杰), Kai Liu(刘凯), Xiao Zhang(张晓)
Chin. Phys. B, 2021, 30 (**5**): 057104. DOI: 10.1088/1674-1056/abec38

Ultra-low Young's modulus and high super-exchange interactions in monolayer CrN: A promising candidate for flexible spintronic applications

Yang Song(宋洋), Yan-Fang Zhang(张艳芳), Jinbo Pan(潘金波), and Shixuan Du(杜世萱)
Chin. Phys. B, 2021, 30 (**4**): 047105. DOI: 10.1088/1674-1056/abdb20

First-principles calculations of F-, Cl-, and N-related defects of amorphous SiO_2 and their impacts on carrier trapping and proton release

Xin Gao(高鑫), Yunliang Yue(乐云亮), Yang Liu(刘杨), and Xu Zuo(左旭)
Chin. Phys. B, 2021, 30 (**4**): 047104. DOI: 10.1088/1674-1056/abe3f7

Passivation of PEA^+ to $MAPbI_3$ (110) surface states by first-principles calculations

Wei Hu(胡伟), Ying Tian(田颖), Hong-Tao Xue(薛红涛), Wen-Sheng Li(李文生), and Fu-Ling Tang(汤富领)
Chin. Phys. B, 2021, 30 (**4**): 047101. DOI: 10.1088/1674-1056/abccb7

Structure prediction, electronic, and mechanical properties of alkali metal MB_{12} (*M= Be*, Mg, Ca, Sr) from first principles

Chun-Ying Pu(濮春英), Rong-Mei Yu(于荣梅), Ting Wang(王婷), Zhen-Yan X\"ue(薛振彦), Yong-Sheng Zhu(朱永胜), and Da-Wei Zhou(周大伟)
Chin. Phys. B, 2021, 30 (**1**): 017102. DOI: 10.1088/1674-1056/abb667

First-principles investigation of the valley and electrical properties of carbon-doped α-graphyne-like BN sheet*

Bo Chen(陈波)†, Xiang-Qian Li(李向前), Lin Xue(薛林),
Yan Han(韩燕), Zhi Yang(杨致), and Long-Long Zhang(张龙龙)

College of Physics and Optoelectronics, Taiyuan University of Technology, Taiyuan 030024, *China*

(Received 17 December 2020; revised manuscript received 14 January 2021; accepted manuscript online 20 January 2021)

Based on *ab initio* density functional theory calculations, we demonstrate that two carbon-doped boron nitride analog of α-graphyne structures, $B_3C_2N_3$ and BC_6N monolayers, are two-dimensional direct wide band gap semiconductors, and there are two inequivalent valleys in the vicinities of the vertices of their hexagonal Brillouin zones. Besides, $B_3C_2N_3$ and BC_6N monolayers exhibit relatively high carrier mobilities, and their direct band gap feature is robust against the biaxial strain. More importantly, the energetically most favorable $B_3C_2N_3$ and BC_6N bilayers also have direct wide band gaps, and valley polarization could be achieved by optical helicity. Finally, we show that BC_6N monolayer might have high efficiency in photo-splitting reactions of water, and a vertical van der Waals heterostructure with a type-II energy band alignment could be designed using $B_3C_2N_3$ and BC_6N monolayers. All the above-mentioned characteristics make $B_3C_2N_3$ and BC_6N monolayers, bilayers, and their heterostructures recommendable candidates for applications in valleytronic devices, metal-free photocatalysts, and photovoltaic cells.

Keywords: first-principles calculations, α-graphyne like structures, valleytronic materials, wide band gap semiconductors

PACS: 71.15.Mb **DOI:** 10.1088/1674-1056/abddac

1. Introduction

Valleytronics, a new field beyond electronics and spintronics, are based on exploiting and manipulating the electron valley degree of freedom, which is the energy extrema in momentum space.[1,2] The most representative valleytronic materials are monolayers of semiconducting transition metal dichalcogenides MX_2 (M = Mo, W; X = S, Se), which have two degenerate yet inequivalent valleys at the corners of their hexagonal Brillouin zones (the K and K' points). And these two inequivalent valleys are connected by time-reversal symmetry. Due to the lack of the inversion symmetry, carriers in these two inequivalent valleys are subject to opposite Berry curvatures,[3] which are gauge-independent pseudovectors that reflect the handedness and geometries of Bloch waves and act like effective magnetic fields in momentum space.[4–6] The opposite Berry curvatures, direct band gap, and angular momentum of the atomic orbitals together contribute to the different optical selection rules for the two valleys, thus permitting the generation of valley polarization by controlling the helicity of light.[7–9] However, the low carrier mobilities (about 200 $cm^2 \cdot V^{-1} \cdot s^{-1}$ for MoS_2 monolayer) and direct-to-indirect band gap transition induced by strain in MX_2 monolayers restrict their practical applications in valleytronics.[10,11] In addition, the restored inversion symmetry in MX_2 bilayers makes Berry curvature zero at any point in the entire Brillouin zone, which prohibits valley polarization in MX_2 bilayers via the circularly polarized light. Therefore new two-dimensional (2D) valleytronic materials with moderate and robust direct band gaps, high carrier mobilities, and inversion asymmetry independent of layer number are remained to be found.

Owing to the inversion asymmetry and direct band gap of about 6.0 eV,[12] honeycomb boron nitride (h-BN) monolayer is an ideal material to realize valleytronics in the ultraviolet region, but its carrier mobility at room temperature is as low as 0.01 $cm^2 \cdot V^{-1} \cdot s^{-1}$.[13] The carrier mobility of h-BN monolayer may be enhanced by carbon doping,[14] along with a tunable band gap from deep ultraviolet to far-infrared spectra, depending on the carbon doping concentration.[15] Like h-BN monolayer, the inversion asymmetric boron nitride analog of α-graphyne (labeled as α-BNyne) monolayer has a direct band gap of 5.428 eV and a low electron mobility of about 132.04 $cm^2 \cdot V^{-1} \cdot s^{-1}$, as shown in Figs. A1, A2 and Table A1 in supplement material. So we wonder if it is possible that carbon doping could increase the carrier mobilities of α-BNyne while maintaining its direct band gap nature and inversion asymmetry, which is worthy of exploration. In this paper, we predict two valleytronic materials, $B_3C_2N_3$ and BC_6N, through *ab initio* density functional theory (DFT) calculations. We show that both $B_3C_2N_3$ and BC_6N monolayers are energetically more stable than α-BNyne, and have direct band gaps of 3.143 eV and 2.683 eV, respectively. The direct band

*Project supported by the Special Foundation for Theoretical Physics Research Program of China (Grant No. 11847065) and the Natural Science Foundation of Shanxi Province, China (Grant No. 201901D211115).

†Corresponding author. E-mail: chenbo@tyut.edu.cn

© 2021 Chinese Physical Society and IOP Publishing Ltd

gap feature is robust against the biaxial strain. Further calculations demonstrate that $B_3C_2N_3$ and BC_6N monolayers exhibit relatively high carrier mobilities, and inversion asymmetry is reserved in the energetically most favorable $B_3C_2N_3$ and BC_6N bilayers. Finally, the capacity of BC_6N monolayer to be a photocatalyst for water splitting and the separation of photogenerated electrons and holes in $B_3C_2N_3$-BC_6N van der Waals heterostructure are revealed.

2. Computational methods

Our DFT calculations are performed by using Vienna *ab initio* simulation package (VASP).[16] Ion–electron interaction is described by the projector augmented wave (PAW) potentials.[17,18] Exchange–correlation between electrons is treated using the generalized gradient approximation (GGA) in Perdew–Burke–Ernzerhof (PBE) form.[19] Three-dimensional periodic boundary conditions are applied, and a vacuum region of 30 Å is incorporated to avoid interactions between neighboring layers. Geometry optimization is done using the conjugated gradient method[20] with a 3×3 supercell (72 atoms) to avoid possible artifacts of single cell calculations.[21] The energy cutoff of the plane waves is set to 700 eV, with an energy precision of 10^{-6} eV. A 3×3×1 Γ centered Monkhorst–Pack grid is used to sample the Brillouin zone (the convergence tests of energy cutoff and number of k-points are shown in Fig. B1 in supplement material). The atomic positions are fully relaxed until the force on each atom is less than 10^{-2} eV/Å. Considering that the GGA usually underestimates the band gap, Heyd–Scuseria–Ernzerhof (HSE06) hybrid functional[22] is adopted to correct the band structures and optical absorption coefficients. Phonon spectra are calculated using a 3×3 supercell approach within the Phonopy code[23] interfaced with density functional perturbation theory[24] implemented in VASP. *Ab initio* molecular dynamics (AIMD) simulations are carried out at room temperature by using canonical ensemble (NVT) with a 4×4 supercell (128 atoms). Each simulation lasts for 6 ps with a time step of 1.0 fs, and the temperature is controlled by applying the Nosé–Hoover algorithm.[25,26] For the $B_3C_2N_3$ and BC_6N bilayers and vertical heterostructures formed by stacking $B_3C_2N_3$ and BC_6N monolayers, van der Waals interaction is included by employing DFT-D3 method.[27,28] The maximally localized Wannier functions are constructed by Wannier90 code,[29] and the Berry curvatures are calculated through WannierTools package.[30] VASPKIT program is used for data post-processing.[31]

3. Results and discussion

3.1. Structures and stabilities

Like carbon-doped γ-BNyne,[32] two carbon-doped α-BNyne structures are studied here. As shown in Fig. 1, $B_3C_2N_3$ is composed of hexagonal carbon rings linked by BN chains, while BC_6N is composed of BN hexagons connected by carbon chains. There are eight atoms in one primitive unit cell. Atoms at the corners of the hexagonal honeycomb are sp^2-hybridized, because the angle of two neighboring bonds of the atoms is 120°; while atoms at the sides of the hexagonal lattice are sp-hybridized, because they are located in a strict straight line with the atoms at the corners. The lattice constants and bond lengths of the optimized geometric structures for $B_3C_2N_3$ and BC_6N monolayers are summarized in Table 1, with α-BNyne included as a control sample (see Fig. A1(a) in supplement material).

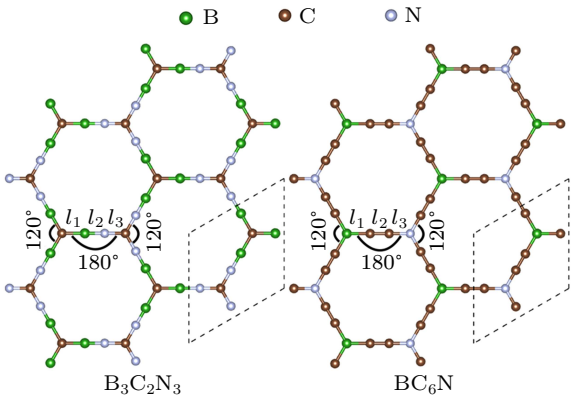


Fig. 1. Top view of $B_3C_2N_3$ and BC_6N monolayers. The dashed line delineates the primitive unit cell.

Table 1. Lattice constant a_0, bond lengths l_1, l_2, and l_3, cohesive energy E_{coh}, calculated elastic constants C_{ij}, Young's modulus Y, and Poisson's ratio ν for $B_3C_2N_3$ and BC_6N monolayers. α-BNyne (B_4N_4) is included for comparison.

$B_xC_yN_z$	a_0 (Å)	Bond length (Å)			E_{coh} (eV/atom)	Elastic constants (N/m)					Y (N/m)	ν
		l_1	l_2	l_3		C_{11}	C_{12}	C_{13}	C_{33}	C_{44}		
$B_3C_2N_3$	7.054	1.469	1.277	1.327	6.201	83.634	77.218	0.053	0.173	0.062	12.340	0.923
BC_6N	7.074	1.507	1.222	1.355	6.415	81.794	71.184	0.019	0.186	0.077	19.844	0.870
B_4N_4	7.108	1.427	1.256	1.421	6.130	80.094	71.284	0.084	0.172	0.046	16.651	0.890

Cohesive energies are calculated to evaluate the energetic stabilities of $B_3C_2N_3$ and BC_6N monolayers using the expression $E_{coh} = (mE_B + nE_C + tE_N - E_{tot})/(m+n+t)$, where $E_B/E_C/E_N$ and E_{tot} are the total energies of an isolated B/C/N atom and a primitive unit cell, respectively. $m/n/t$ is the number of B/C/N atoms in the primitive unit cell. As displayed in Table 1, the cohesive energies of $B_3C_2N_3$ and BC_6N monolayers are higher than that of α-BNyne, indicating that $B_3C_2N_3$ and BC_6N monolayers are substantially more stable than α-BNyne. The mechanical stabilities of $B_3C_2N_3$ and BC_6N

monolayers are assessed on the basis of Born criteria.[33] Due to the added relation $C_{66} = (C_{11} - C_{12})/2$, there are five independent elastic constants in the hexagonal crystal system, and the necessary and sufficient conditions for elastic stability can be derived by calculating the eigenvalues of the stiffness matrix. For mechanically stable 2D hexagonal materials, the following conditions must be met: $C_{11} > |C_{12}|$, $2C_{13}^2 < C_{33} \times (C_{11} + C_{12})$, $C_{44} > 0$. According to our results shown in Table 1, the computed elastic constants satisfy the Born criteria, which indicates that both the $B_3C_2N_3$ and BC_6N monolayers are mechanically stable. Furthermore, 2D Young's modulus (in-plane stiffness) Y and Poisson's ratio ν can be deduced as $Y = (C_{11}^2 - C_{12}^2)/C_{11}$ and $\nu = C_{12}/C_{11}$.[34] The calculated Young's modulus for graphene is 338.609 N/m, which is in accordance with the experimental result of 340 N/m.[35] This supports the reliability of the procedure we employed. As reported in Table 1, it seems that the Young's modulus and Poisson's ratio of α-BNyne are more affected when doping carbon atoms at sp^2-positions, which may be attributed to the one more bond of sp^2-site compared to sp-site. Similar to α-BNyne,[36] $B_3C_2N_3$ and BC_6N monolayers are also soft materials and may have a large deformation under a low stress. The dynamic stabilities of $B_3C_2N_3$ and BC_6N monolayers are evaluated by calculating the phonon spectra displayed in Figs. 2(a) and 2(b). Because of the neglectable contribution of imaginary phonon frequencies in the entire Brillouin zone, $B_3C_2N_3$ and BC_6N monolayers are confirmed to be dynamically stable. Additionally, AIMD simulations at room temperature are performed to investigate the thermal stability of $B_3C_2N_3$ and BC_6N monolayers. As seen from Figs. 2(c) and 2(d), structural integrity could be maintained well at the end of the simulation, demonstrating the promising thermal stability of $B_3C_2N_3$ and BC_6N monolayers. Atoms of $B_3C_2N_3$ or BC_6N monolayer at room temperature are not on the same plane, which is a common characteristic for 2D materials to resist the thermal perturbation via fluctuation.

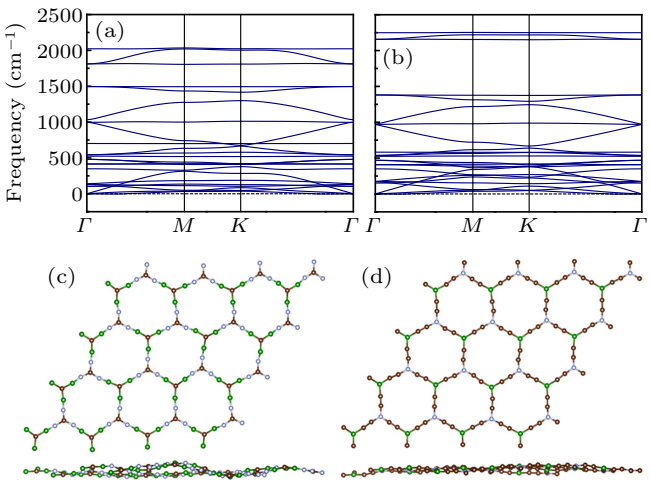


Fig. 2. Phonon dispersions of (a) $B_3C_2N_3$ and (b) BC_6N monolayers, as well as snapshots for the final configurations of (c) $B_3C_2N_3$ and (d) BC_6N monolayers at room temperature.

3.2. Electronic and valley-related physical properties of $B_3C_2N_3$ and BC_6N monolayers

After confirming the excellent stabilities of $B_3C_2N_3$ and BC_6N monolayers, we wonder whether they have a sizeable direct band gap just like α-BNyne. As exhibited in Figs. 3(a) and 3(b), both $B_3C_2N_3$ and BC_6N monolayers are nonmagnetic semiconductors with direct band gaps of 3.143 eV and 2.683 eV, respectively, calculated at the HSE06 level of theory. The valence band maximum (VBM) and conduction band minimum (CBM) of $B_3C_2N_3$/BC_6N monolayer are located at the K point in the Brillouin zone. For $B_3C_2N_3$ monolayer, the partial density of states (PDOS) shows that the valence bands near the Fermi level are predominantly composed of p_z orbitals of N atoms and the C atoms surrounded by B atoms, while the conduction bands close to the Fermi level are mainly consisted of p_z orbitals of B atoms and the C atoms surrounded by N atoms. This is further confirmed by the isosurfaces of charge densities of VBM and CBM as illustrated in Fig. 3(c). For BC_6N monolayer, PDOS and isosurfaces of charge densities of VBM and CBM (Fig. 3(d)) reveal that the valence bands around the Fermi level are predominantly composed of p_z orbitals of N atoms and C atoms at the carbon chains, while the conduction bands in the vicinity of the Fermi level are mainly consisted of p_z orbitals of B atoms and the C atoms that surround the N atoms. So $B_3C_2N_3$ and BC_6N monolayers are two-dimensional direct wide band gap semiconductors. The larger band gap of $B_3C_2N_3$ monolayer compared to that of BC_6N monolayer may due to the larger electronegativity difference between B and N in $B_3C_2N_3$ than that between B and C or between N and C in BC_6N.[37,38] Interestingly, the charge density of VBM/CBM of $B_3C_2N_3$ monolayer looks like that of CBM/VBM of BC_6N monolayer. This possibly leads to opposite responses of band gaps to biaxial strain, which we will discuss later.

Similar to semiconducting MX_2 monolayers, the time-reversal symmetry and the inversion asymmetry make $B_3C_2N_3$/BC_6N monolayer have two energy-degenerate but inequivalent valleys at the corners of the first Brillouin zone, namely, the K and K' valleys, and these two valleys have opposite Berry curvatures. According to Kubo formula,[39–41] Berry curvature $\Omega(\boldsymbol{k})$ can be written as

$$\Omega(\boldsymbol{k}) = \sum_n f_n \Omega_n(\boldsymbol{k}), \tag{1}$$

$$\Omega_n(\boldsymbol{k}) = -\sum_{n' \neq n} \frac{2\,\mathrm{Im}\langle \psi_{n\boldsymbol{k}} | v_x | \psi_{n'\boldsymbol{k}} \rangle \langle \psi_{n'\boldsymbol{k}} | v_y | \psi_{n\boldsymbol{k}} \rangle}{(E_{n'} - E_n)^2}, \tag{2}$$

where $|\psi_{n\boldsymbol{k}}\rangle$ is the Bloch function with eigenvalue E_n, f_n is the Fermi–Dirac distribution function, and $v_{x(y)}$ are the velocity operators. The Berry curvatures of the occupied states for $B_3C_2N_3$ and BC_6N monolayers are obtained through constructing the maximally localized Wannier functions, as seen in Fig. 4(a).

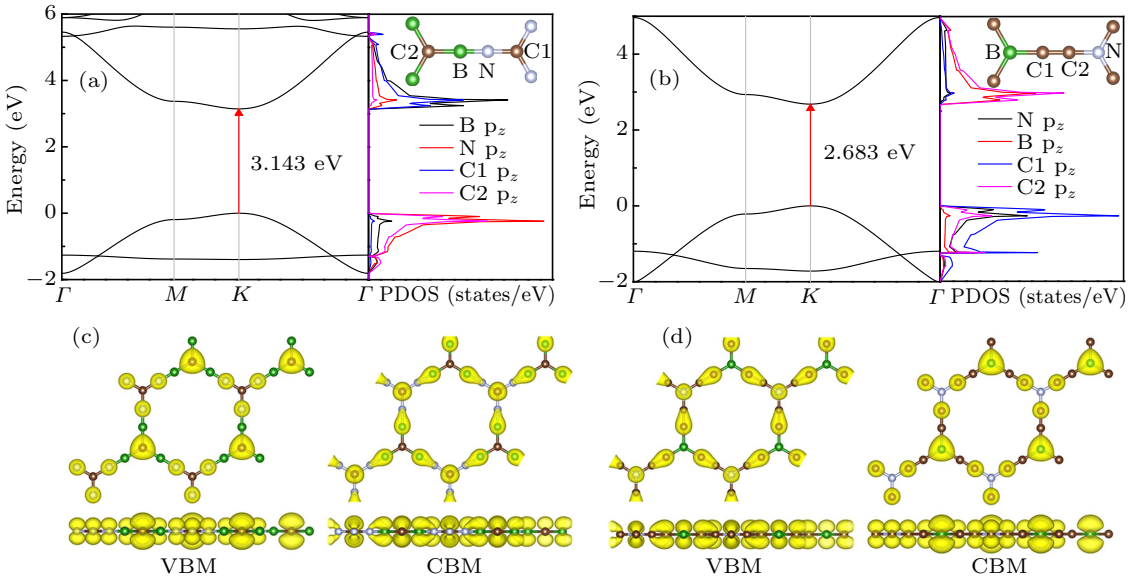


Fig. 3. Band structures and PDOSs obtained within the HSE06 scheme for (a) $B_3C_2N_3$ and (b) BC_6N monolayers, the VBM is set to 0 eV. Charge densities of VBM and CBM states for (c) $B_3C_2N_3$ and (d) BC_6N monolayers.

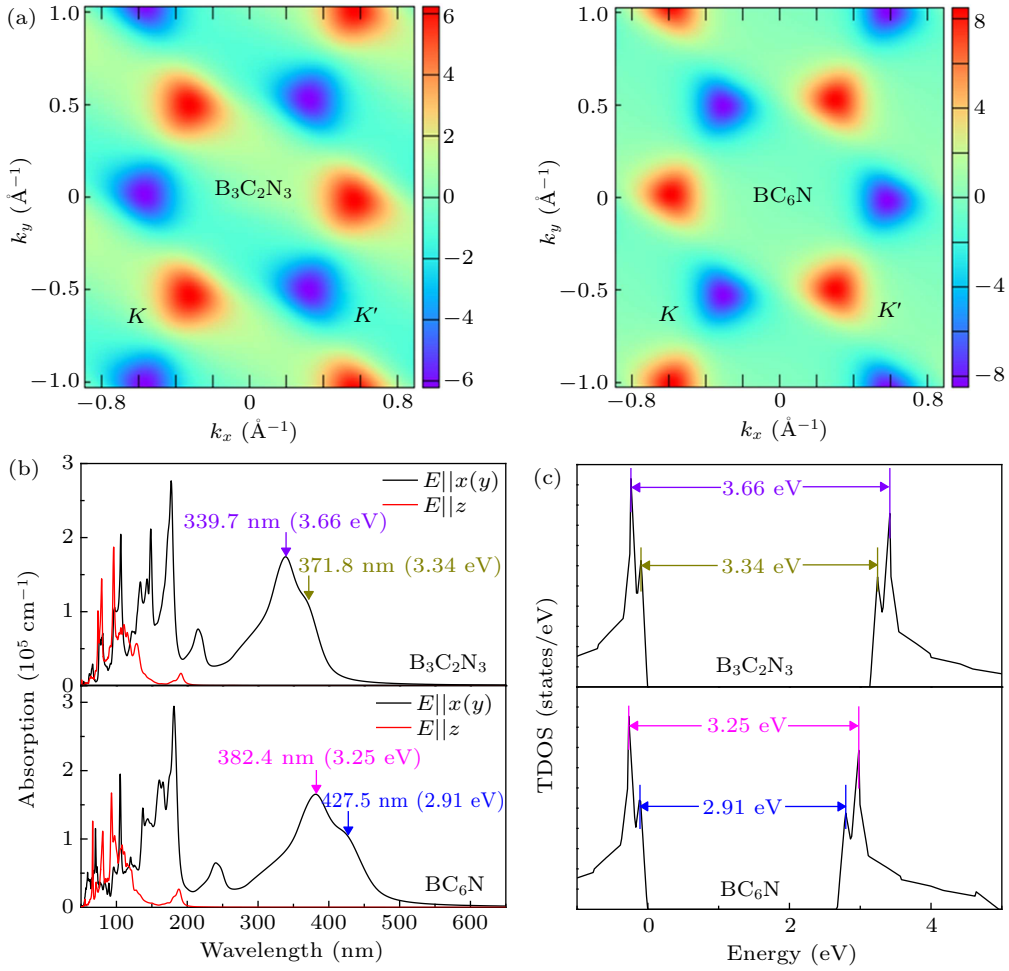


Fig. 4. (a) Berry curvatures, (b) absorption coefficients, and (c) TDOSs of $B_3C_2N_3$ and BC_6N monolayers, where the absorption coefficients and TDOSs are calculated with the HSE06 hybrid functional.

Obviously, the Berry curvatures at K and K' valleys exhibit obvious peaks but with opposite signs, and the distribution of Berry curvatures shows C_{3v} symmetry. So although the electrons in the neighboring valleys have the same energy, they can be distinguished by their opposite Berry curvatures. Meanwhile, for the incident light with the electric field ($\boldsymbol{E}$) polarized along the x, y ($\boldsymbol{E}\perp z$), and z ($\boldsymbol{E} \parallel z$) directions, absorption coefficients $\alpha(\omega)$ can be calculated according to the

formula:[42]

$$\alpha(\omega) = \frac{\sqrt{2}\omega}{c}\left\{\left[\varepsilon_1^2(\omega)+\varepsilon_2^2(\omega)\right]^{1/2}-\varepsilon_1(\omega)\right\}^{1/2}, \quad (3)$$

where $\varepsilon_1(\omega)$ and $i\varepsilon_2(\omega)$ are the real and imaginary parts of the dielectric function $\varepsilon(\omega)$ ($\varepsilon(\omega) = \varepsilon_1(\omega) + i\varepsilon_2(\omega)$), c is the magnitude of light velocity in vacuum, and ω is the circular frequency of the incident light. As depicted in Fig. 4(b), we find that the absorption coefficients are the same for polarization along the x and y directions, which may indicate the isotropic in-plane optical properties. Both the $B_3C_2N_3$ and BC_6N monolayers have two high in-plane absorption peaks in the 300–450 nm region, which may be caused by the transitions between the corresponding peaks in the total density of states (TDOS) displayed in Fig. 4(c), as the transition probability of electrons is proportional to the TDOS.[43] Hence, the direct band gaps, valley-contrasting Berry curvatures, together with the large absorption coefficients make valley polarization in $B_3C_2N_3$ and BC_6N monolayers achievable via valley-selective circular dichroism.[9]

For $B_3C_2N_3$ and BC_6N monolayers utilized in valleytronics, two requirements must be met. One is that $B_3C_2N_3$ and BC_6N monolayers should have relatively high carrier mobilities. The other is that the direct band gap nature can be maintained under strain, because $B_3C_2N_3$ and BC_6N monolayers are soft materials and may have a large deformation under a low stress, as mentioned above. The carrier mobilities of electrons and holes for $B_3C_2N_3$ and BC_6N monolayers are calculated based on the deformation potential theory,[44] which has been extensively used to evaluate the carrier mobilities of 2D materials.[45,46] For inorganic semiconductors, the coherent wavelength of thermally activated electrons or holes is comparable to the wavelength of acoustic phonon and is much longer than the typical bond length, so the scattering of a thermal electron or hole is dominated by the electron–acoustic phonon coupling. On the basis of effective mass approximation, the carrier mobility in 2D materials can be expressed as

$$\mu_{2D} = \frac{2e\hbar^3 C_{2D}}{3k_B T|m^*|^2 E_d^2}, \quad (4)$$

where e, k_B, T, $\hbar$, and m^* are the electron charge, Boltzmann constant, temperature, reduced Planck constant, and carrier effective mass, respectively. C_{2D} is the elastic modulus defined as $C_{2D} = (\partial^2 E_{2D}/\partial\delta^2)/S_0$, in which E_{2D} is the total energy of the system, S_0 represents the area of the optimized structure. δ is the applied biaxial strain and is defined by $(a-a_0)/a_0$, here a_0 and a are the optimized lattice constant and the lattice length along the strain direction, respectively. Negative and positive values of strain stand for the compression and elongation, respectively. E_d is the deformation potential constant denoting the shift of the band edges (CBM for electrons and VBM for holes) induced by the strain. For $B_3C_2N_3$ and BC_6N monolayers, the changes of total energies and band edges with biaxial strain are illustrated in Fig. C1 in supplement material, and the obtained C_{2D}, E_d, m^*, μ at 300 K for $B_3C_2N_3$ and BC_6N monolayers are compiled in Table 2. It should be noted that the shift of the VBM for $B_3C_2N_3$ monolayer is small and is not linear with the biaxial strain, as shown in Fig. C1(a). The reason is unclear now, which needs further research. Compared to the electron mobility of 132.04 $cm^2\cdot V^{-1}\cdot s^{-1}$ and hole mobility of 1527.16 $cm^2\cdot V^{-1}\cdot s^{-1}$ for α-BNyne, doping carbon atoms at the corner could increase the electron mobility by about four times, while doping carbon atoms at the side of hexagonal lattice could greatly enhance the electron mobility and maintain the hole mobility. So doping carbon atoms in α-BNyne would increase the carrier mobilities. $B_3C_2N_3$ and BC_6N monolayers exhibit relatively high carrier mobilities.

Table 2. Calculated elastic modulus C_{2D}, deformation potential constant E_d, effective mass m^*, carrier mobility μ at 300 K for $B_3C_2N_3$ and BC_6N monolayers. m_0 is the mass of free electron. E_d and m^* are obtained by the HSE06 method.

$B_xC_yN_z$	Carrier type	C_{2D} (eV/Å^2)	E_d (eV)	m^* (m_0)	μ ($cm^2\cdot V^{-1}\cdot s^{-1}$)
$B_3C_2N_3$	electron	20.08	–7.35	0.39	545.79
	hole		–	0.47	–
BC_6N	electron	19.12	–3.58	0.36	2652.21
	hole		–3.78	0.42	1740.95

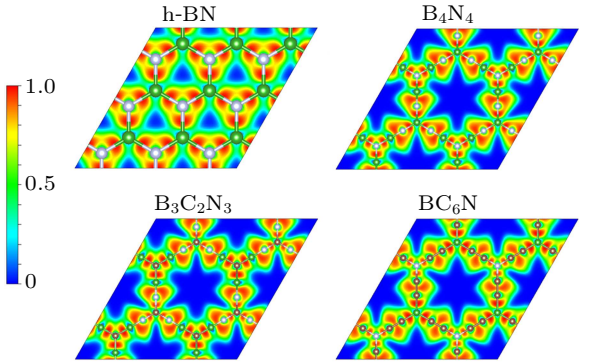


Fig. 5. Electron localization function maps for h-BN, α-BNyne (B_4N_4), $B_3C_2N_3$, and BC_6N.

Why carbon doping can increase the electron mobility of α-BNyne? For h-BN, the large electronegativity difference between B and N makes the B–N bond ionic.[47,48] So electrons are bound to the N atoms, as demonstrated by the electron localization function (ELF) map of h-BN shown in Fig. 5. This causes the low electron mobility and large band gap in h-BN. Like h-BN, electrons are also bound to the N atoms in α-BNyne, hence its electron mobility is low and its band gap is large. Furthermore, from ELF map of α-BNyne we can find that the sp-hybridized N atoms at the sides of hexagonal lattice have stronger ionic nature compared to the sp^2-hybridized N atoms at the corners of hexagonal honeycomb. When doping carbon atoms into α-BNyne, its intermediate electronegativity between those of B and N atoms makes the B–C and C–N bonds have stronger covalent nature and weaker

ionic properties than the B–N bond, as verified by the ELF maps of $B_3C_2N_3$ and BC_6N monolayers in Fig. 5. So electrons in $B_3C_2N_3$ and BC_6N monolayers are less bound and more mobile compared with the electrons in α-BNyne. More significantly, there are no sp-hybridized N atoms in BC_6N monolayer, thus it has high electron mobility over the $B_3C_2N_3$ monolayer.

Interestingly, from Table 2 and Fig. C1 we can find that in $B_3C_2N_3$ monolayer, the shift of CBM is quit dependent on the biaxial strain, contrary to the basically independence of VBM on biaxial strain. But in BC_6N monolayer, the absolute value of E_d for VBM is little larger than that for CBM. So with the increase of biaxial strain, band gap for $B_3C_2N_3$ monolayer should decrease while band gap for BC_6N monolayer should increase, and the rangeability of band gap of $B_3C_2N_3$ monolayer is larger than that of band gap of BC_6N monolayer. To prove our deduction, biaxial strain dependent band structures and band gaps of $B_3C_2N_3$ and BC_6N monolayers are calculated by using the HSE06 functional, as presented in Figs. C2, C3 and 6. It can be seen that the locations of VBM and CBM are at K point in the Brillouin zone and do not move within a strain range from -2% to 2%, indicating that the direct band gap feature of $B_3C_2N_3$ and BC_6N monolayers is robust against the biaxial strain. Changes of band gaps for $B_3C_2N_3$ and BC_6N monolayers are opposite and agree with our inference. We attribute this to the fact that $B_3C_2N_3$ and BC_6N monolayers have inverse charge density distributions at the band edges, which may result in the opposite responses of the band gaps to biaxial strain.

In addition, band edges of $B_3C_2N_3$ and BC_6N monolayers can straddle the redox potentials of water (at pH = 0, the standard oxidation potential of H_2O/O_2 is -5.67 eV, and reduction potential of H^+/H_2 is -4.44 eV. Vacuum level is set to zero for reference),[49] but the band gap of $B_3C_2N_3$ monolayer is too large for efficient solar energy absorption. So BC_6N monolayer might be a promising candidate photocatalyst for practical applications in visible-light-driven water splitting.

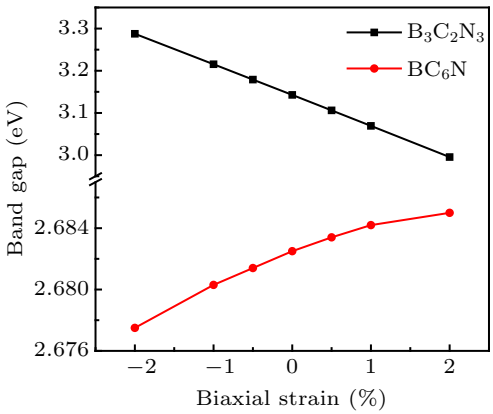


Fig. 6. Band gaps as a function of biaxial strain for $B_3C_2N_3$ and BC_6N monolayers.

3.3. Bilayers and heterostructures

Since $B_3C_2N_3$ and BC_6N monolayers are valleytronic materials, we address the question of whether $B_3C_2N_3$ and BC_6N bilayers can also be utilized in valleytronics, or not. Like α-BNyne bilayer,[50] five different high symmetry stacking configurations are proposed and investigated for $B_3C_2N_3$ and BC_6N bilayers, as shown in Fig. 7.

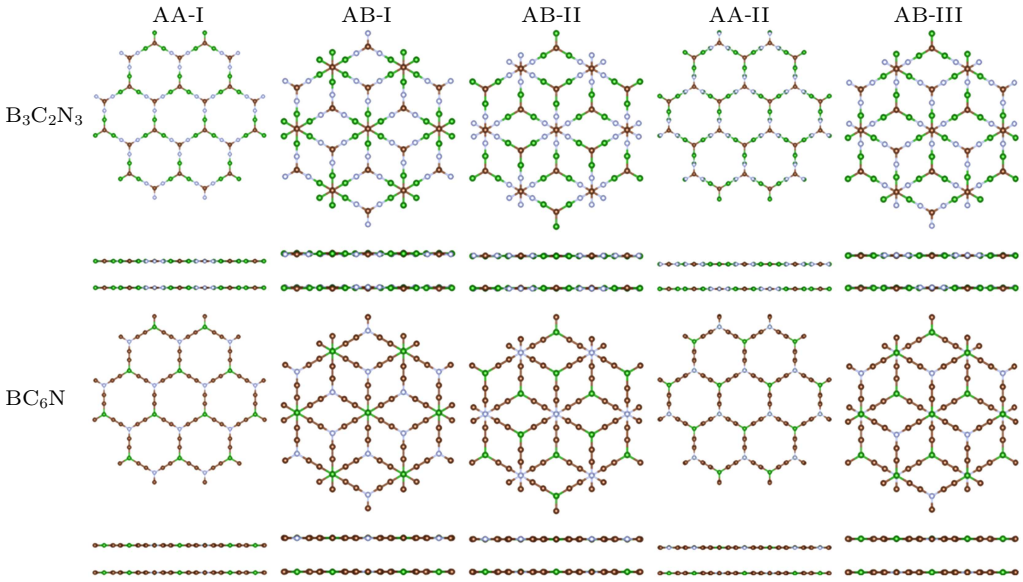


Fig. 7. Top and side views for the different stacking configurations of $B_3C_2N_3$ and BC_6N bilayers.

In AA-I and AA-II configurations, hexagons in both layers face each other; while in AB-I, AB-II, and AB-III configurations, the first layer is shifted laterally to the centers of hexagons in the second layer. The optimized lattice constant a_0, interlayer distance d_z, and interlayer binding energy E_b^{Bi} for $B_3C_2N_3$ and BC_6N bilayers with different stacking configura-

tions are summarized in Table D1. The interlayer binding energy is defined as $E_b^{Bi} = (E_{bi} - 2E_{mo})/S$, where E_{bi}/E_{mo} and S are the total energy of the bilayer/monolayer and the coupling area, respectively. As listed in Table D1, the lattice parameters differ slightly for different stacking types, and the negative value of E_b^{Bi} indicates that the stacking process is exothermic. Coincidentally, the AB-III configuration is energetically most favorable for both the $B_3C_2N_3$ and BC_6N bilayers. The band structures and Berry curvatures for AB-III stacking $B_3C_2N_3$ and BC_6N bilayers are illustrated in Fig. 8. Similar to the monolayer, the energetically most stable $B_3C_2N_3$ and BC_6N bilayers also have direct wide band gaps at K point in the Brillouin zone and possess the non-zero valley-contrasting Berry curvatures. So optical emission polarization in $B_3C_2N_3$ and BC_6N bilayers with AB-III stacking mode could also be realized by selective valley excitation.

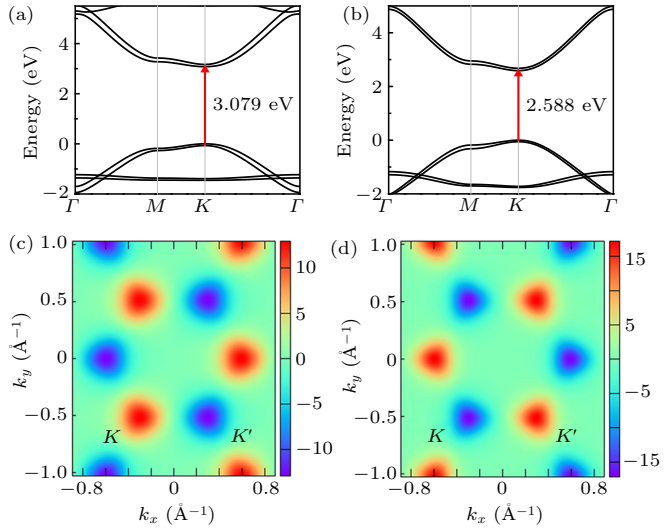


Fig. 8. (a)/(b) Band structure (HSE06) and (c)/(d) Berry curvature for $B_3C_2N_3/BC_6N$ bilayer with AB-III configuration.

Figure C1 shows that the heterostructure constructed by stacking $B_3C_2N_3$ and BC_6N monolayers has a type-II energy band alignment, which could spontaneously separate the free electrons and holes and is suitable for optoelectronics and solar energy conversion. Owing to the similar lattice constants of $B_3C_2N_3$ and BC_6N monolayers as represented in Table 1, $B_3C_2N_3$-BC_6N van der Waals heterostructures in six different stacking orders are considered, as shown in Fig. 9. The optimized lattice constant a_0, interlayer distance d_z, and interlayer binding energy E_b^{Hete} for $B_3C_2N_3$–BC_6N van der Waals heterostructures with different stacking models are summarized in Table D2, which shows that the AB-I stacking is energetically most stable. For heterostructures studied here, the interlayer binding energy is defined as $E_b^{Hete} = (E_{hete} - E_1 - E_2)/S$, where E_{hete}, E_1, and E_2 represent the total energy of the heterostructure, $B_3C_2N_3$ monolayer, and BC_6N monolayer, respectively. S is the coupling area. As illustrated in Fig. 10, the AB-I stacking $B_3C_2N_3$–BC_6N van der Waals heterostructure also has a direct wide band gap, with electrons confined in BC_6N while holes confined in $B_3C_2N_3$. It is, therefore, expected that spontaneous charge separation occurs when the heterostructure absorbs photons with photon energy larger than 2.528 eV, a process which will substantially reduce the possibility of electron–hole recombination and is needed for photovoltaics.

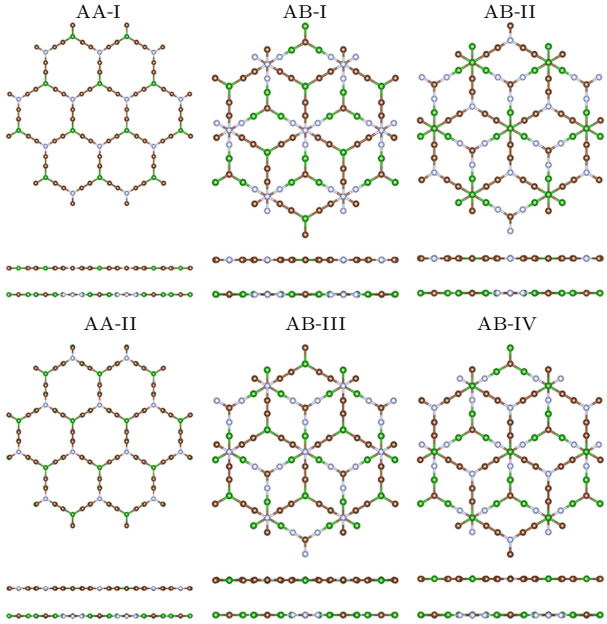


Fig. 9. Top and side views for the $B_3C_2N_3$–BC_6N van der Waals heterostructures in six different stacking orders.

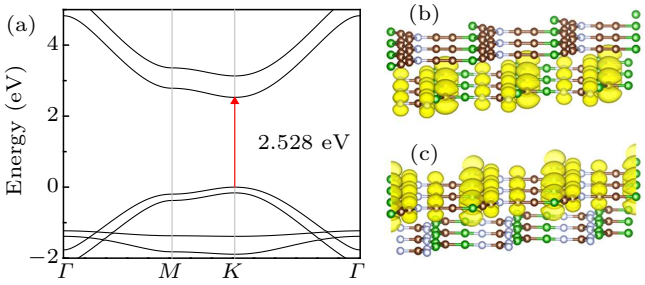


Fig. 10. (a) Band structure and charge densities of (b) VBM and (c) CBM states for AB-I stacking $B_3C_2N_3$-BC_6N van der Waals heterostructure.

4. Conclusions

Using first-principles calculations, we demonstrate that carbon doping can increase the carrier mobilities of α-BNyne while maintain its direct band gap nature and inversion asymmetry, which make the two carbon-doped α-BNyne structures, namely, the $B_3C_2N_3$ and BC_6N monolayers, potential valleytronic materials. More importantly, unlike the MoS_2 bilayer, optical pumping with circularly polarized light might achieve valley polarization in the energetically most favorable $B_3C_2N_3$ and BC_6N bilayers. Besides, the promising photocatalytic activity of BC_6N monolayer for efficient solar water splitting and the type-II energy band alignment between

$B_3C_2N_3$ and BC_6N monolayers are revealed.

We should note that except for α-BNyne, β-, γ-, and 6, 6, 12-BNyne are all direct wide band gap semiconductors with inversion asymmetry,[51] and the valley properties are affected by temperature and magnetic field.[52,53] So do these materials have relatively high carrier mobilities? If not, can carbon doping increase their carrier mobilities and make them suitable for applications in valleytronics? What is the influence of temperature and magnetic field on the valley properties of $B_3C_2N_3$ and BC_6N monolayers? Can valley splitting be realized in the heterostructure formed by stacking $B_3C_2N_3$/BC_6N monolayer with a ferromagnetic material? These are worthy of exploration. Further researches are in progress.

References

[1] Schaibley J R, Yu H Y, Clark G, Rivera P, Ross J S, Seyler K L, Yao W and Xu X D 2016 *Nat. Rev. Mater.* **1** 16055
[2] Xu X D, Yao W, Xiao D and Heinz T F 2014 *Nat. Phys.* **10** 343
[3] Xiao D, Liu G B, Feng W X, Xu X D and Yao W 2012 *Phys. Rev. Lett.* **108** 196802
[4] Xiao D, Yao W and Niu Q 2007 *Phys. Rev. Lett.* **99** 236809
[5] Yao W, Xiao D and Niu Q 2008 *Phys. Rev. B* **77** 235406
[6] Xiao D, Chang M C and Niu Q 2010 *Rev. Mod. Phys.* **82** 1959
[7] Mak K F, He K L, Shan J and Heinz T F 2012 *Nat. Nanotechnol.* **7** 494
[8] Zeng H L, Dai J F, Yao W, Xiao D and Cui X D 2012 *Nat. Nanotechnol.* **7** 490
[9] Cao T, Wang G, Han W P, Ye H Q, Zhu C R, Shi J R, Niu Q, Tan P H, Wang E G, Liu B L and Feng J 2012 *Nat. Commun.* **3** 887
[10] Radisavljevic B, Radenovic A, Brivio J, Giacometti V and Kis A 2011 *Nat. Nanotechnol.* **6** 147
[11] Yun W S, Han S W, Hong S C, Kim I G and Lee J D 2012 *Phys. Rev. B* **85** 033305
[12] Singh R S, Tay R Y, Chow W L, Tsang S H, Mallick G and Teo E H T 2014 *Appl. Phys. Lett.* **104** 163101
[13] Mahvash F, Paradis E, Drouin D, Szkopek T and Siaj M 2015 *Nano Lett.* **15** 2263
[14] Kaloni T P, Joshi R P, Adhikari N P and Schwingenschlogl U 2014 *Appl. Phys. Lett.* **104** 073116
[15] Song Z G, Lips Z W, Wang H, Bai X D, Wang W L, Du H L, Liu S Q, Wang C S, Han J Z, Yang Y C, Liu Z, Lu J, Fang Z Y and Yang J B 2017 *Nano Lett.* **17** 2079
[16] Kresse G and Furthmüller J 1996 *Comput. Mater. Sci.* **6** 15
[17] Blöchl P E 1994 *Phys. Rev. B* **50** 17953
[18] Kresse G and Joubert D 1999 *Phys. Rev. B* **59** 1758
[19] Perdew J P, Burke K and Ernzerhof M 1996 *Phys. Rev. Lett.* **77** 3865
[20] Hestenes M R and Stiefel E 1952 *J. Res. Natl. Bur. Stand.* **49** 409
[21] Özçelik V O, Aktürk O Ü, Durgun E and Ciraci S 2015 *Phys. Rev. B* **92** 125420
[22] Heyd J, Scuseria G E and Ernzerhof M 2003 *J. Chem. Phys.* **118** 8207
[23] Togo A, Oba F and Tanaka I 2008 *Phys. Rev. B* **78** 134106
[24] Gonze X and Lee C 1997 *Phys. Rev. B* **55** 10355
[25] Nóse S 1984 *J. Chem. Phys.* **81** 511
[26] Hoover W G 1985 *Phys. Rev. A* **31** 1695
[27] Grimme S, Antony J, Ehrlich S and Krieg H 2010 *J. Chem. Phys.* **132** 154104
[28] Grimme S, Ehrlich S and Goerigk L 2011 *J. Comput. Chem.* **32** 1456
[29] Marzari N and Vanderbilt D 1997 *Phys. Rev. B* **56** 12847
[30] Wu Q S, Zhang S N, Song H F, Troyer M and Soluyanov A A 2018 *Comput. Phys. Commun.* **224** 405
[31] Wang V, Xu N, Liu J C, Tang G and Geng W T 2019 arXiv:1908.08269
[32] Singh N B, Bhattacharya B and Sarkar U 2014 *Struct. Chem.* **25** 1695
[33] Mouhat F and Coudert F X 2014 *Phys. Rev. B* **90** 224104
[34] Jiao L, Hu M, Peng Y, Luo Y, Li C and Chen Z 2016 *J. Solid State Chem.* **244** 120
[35] Lee C, Wei X D, Kysar J W and Hone J 2008 *Science* **321** 385
[36] Özçelik V O and Ciraci S 2013 *J. Phys. Chem. C* **117** 2175
[37] Di Quarto F, Sunseri C, Piazza S and Romano M C 1997 *J. Phys. Chem. B* **101** 2519
[38] Qiao L, Zhang S, Xiao H Y, Singh D J, Zhang K H L, Liu Z J, Zu X T and Li S 2018 *J. Mater. Chem. C* **6** 1239
[39] Thouless D J, Kohmoto M, Nightingale M P and den Nijs M 1982 *Phys. Rev. Lett.* **49** 405
[40] Yao Y, Kleinman L, MacDonald A H, Sinova J, Jungwirth T, Wang D S, Wang E and Niu Q 2004 *Phys. Rev. Lett.* **92** 037204
[41] Feng W X, Yao Y G, Zhu W G, Zhou J J, Yao W and Xiao D 2012 *Phys. Rev. B* **86** 165108
[42] Peng B, Zhang H, Shao H Z, Xu Y F, Zhang R J and Zhua H Y 2016 *J. Mater. Chem. C* **4** 3592
[43] Luo Y Z, Hu Y B and Xie Y Q 2019 *J. Mater. Chem. A* **7** 27503
[44] Bardeen J and Shockley W 1950 *Phys. Rev.* **80** 72
[45] Chen J M, Xi J Y, Wang D and Shuai Z G 2013 *J. Phys. Chem. Lett.* **4** 1443
[46] Phuc H V, Hieu N N, Hoi B D, Hieu N V, Thu T V, Hung N M, Ilyasov V V, Poklonski N A and Nguyen C V 2018 *J. Electron. Mater.* **47** 730
[47] ahin H, Cahangirov S, Topsakal M, Bekaroglu E, Akturk E, Senger R T and Ciraci S 2009 *Phys. Rev. B* **80** 155453
[48] Zheng H, Li X B, Chen N K, Xie S Y, Tian W Q, Chen Y P, Xia H, Zhang S B and Sun H B 2015 *Phys. Rev. B* **92** 115307
[49] Chakrapani V, Angus J C, Anderson A B, Wolter S D, Stoner B R and Sumanasekera G U 2007 *Science* **318** 1424
[50] Behzad S 2016 *Solid State Commun.* **248** 27
[51] Zhang Y N, Yun J N, Wang K Y, Chen X H, Yang Z, Zhang Z Y, Yan J F and Zhao W 2017 *Comput. Mater. Sci.* **136** 12
[52] Sun S B, Dan J C, Xie X, Yu Y, Yang L L, Xiao S, Wu S Y, Peng K, Song F L, Wang Y N, Yang J N, Qian C J, Zuo Z C and Xu X L 2020 *Chin. Phys. Lett.* **37** 087801
[53] Xu L X, Lu W G, Hu C, Guo Q X, Shang S, Xu X L, Yu G H, Yan Y, Wang L H and Teng J 2020 *Chin. Phys. B* **29** 077304